2021

Templated Growth of a Spin-Frustrated Cluster Fragment of MnBr2 in a MetalOrganic Framework

Turkiewicz, Ari; Tomlinson, Warren; Gonzalez, Miguel I.; Hooper, Joseph P.; Long, Jeffrey R.

American Chemical Society

Turkiewicz, Ari, et al. "Templated Growth of a Spin-Frustrated Cluster Fragment of MnBr2 in a MetalOrganic Framework." Inorganic Chemistry 60.21 (2021): 16103-16110.
http://hdl.handle.net/10945/69323

Inorganic Chemistry

pubs.acs.org/IC Article

Templated Growth of a Spin-Frustrated Cluster Fragment of $MnBr_2$ in a Metal–Organic Framework

Ari Turkiewicz, Warren Tomlinson, Miguel I. Gonzalez, Joseph P. Hooper, and Jeffrey R. Long*

Cite This: *Inorg. Chem.* 2021, 60, 16103–16110 Read Online

ACCESS | Metrics & More | Article Recommendations | Supporting Information

ABSTRACT: The metal–organic framework $Zr_6O_4(OH)_4(bpydc)_6$ ($bpydc^{2-}$ = 2,2′-bipyridine-5,5′-dicarboxylate) is used to template the growth of a cluster fragment of the two-dimensional solid $MnBr_2$, which was predicted to exhibit spin frustration. Single-crystal and powder X-ray diffraction analyses reveal a cluster with 19 metal ions arranged in a triangular lattice motif. Static magnetic susceptibility measurements indicate antiferromagnetic coupling between the high-spin ($S = {}^5/_2$) Mn^{II} centers, and dynamic magnetic susceptibility data suggest population of low-lying excited states, consistent with magnetic frustration. Density functional theory calculations are used to determine the energies for a subset of thousands of magnetic configurations available to the cluster. The Yamaguchi generalized spin-projection method is then employed to construct a model for magnetic coupling interactions within the cluster, enabling facile determination of the energy for all possible magnetic configurations. The confined cluster is predicted to possess a doubly degenerate, highly geometrically frustrated ground state with a total spin of $S_{Total} = {}^5/_2$.

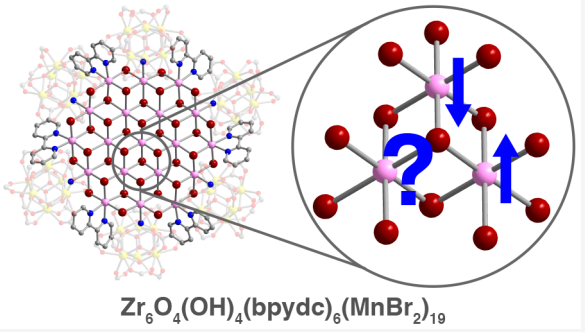

INTRODUCTION

Magnetic molecules exhibiting spin frustration have gained increasing attention for hosting unique physical properties.[1] For instance, the chiral spin states of frustrated triangular clusters have been proposed as an alternative means for encoding spin qubits.[2,3] Additionally, these molecules can serve as models for bulk materials, supplementing our understanding of nontrivial magnetic order in spin-frustrated systems such as spin liquids.[4,5]

Geometric spin frustration arises in both molecules and bulk materials because of competing antiferromagnetic interactions that cannot be simultaneously satisfied. For example, two-dimensional triangular[6] and Kagomé[7,8] lattices and three-dimensional hyper-Kagomé[9] and pyrochlore[10] lattices can all provide platforms for studying spin frustration in bulk materials. In addition, molecular systems featuring odd-numbered metal rings,[11] cuboctahedra and icosidodecahedra,[12,13] and disklike clusters with triangular motifs[14−20] have all demonstrated spin-frustration effects. The magnitude of the spin on the individual magnetic centers themselves is also important in these frustrated systems. For spin liquids, most research has focused on magnetic centers with spin, S, or total angular momentum, J, values of ${}^1/_2$, which are least likely to afford long-range-ordered, commensurate ground states.[6−10] However, higher-spin systems can also afford interesting phenomena such as spin chirality.[21]

Recently, we reported a series of metal halide clusters of the type $M_{19}X_{38}$ (M = Fe, Co, Ni; X = Cl, Br) confined within the metal–organic framework $Zr_6O_4(OH)_4(bpydc)_6$ (**1**; $bpydc^{2-}$ = 2,2′-bipyridine-5,5′-dicarboxylate).[22] Notably, single-crystal X-ray diffraction characterization of all of the clusters revealed a triangular lattice akin to a single layer of the corresponding bulk metal dihalide. The intralayer ferromagnetic coupling characteristic of the bulk metal halides is also retained in these clusters and gives rise to high-spin ground states. Given the close relationship between the atomic and magnetic structures of these clusters and those of their parent materials, we sought to assemble analogous framework-confined clusters with antiferromagnetically coupled metal ions to prepare a magnetically frustrated system. We identified $MnBr_2$ as a promising target, given that it is a bulk antiferromagnet constructed from $S_{Mn} = {}^5/_2$ spin centers on a triangular lattice and it crystallizes in the layered CdI_2 structure type.[23] Of note, although they have not yet been isolated, monolayers of $MnBr_2$ are predicted to be exfoliable, antiferromagnetic semiconductors.[24] Moreover, lateral confinement of two-dimensional monolayers is emerging as a powerful handle to modulate the electromagnetic properties.[25,26] While several Mn-based, disklike clusters have been reported, most are hydroxo-bridged, mixed-valent clusters that have been designed to maximize spin rather

Received: May 3, 2021
Published: October 10, 2021

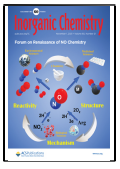

https://doi.org/10.1021/acs.inorgchem.1c01345
Inorg. Chem. 2021, 60, 16103–16110

than to engender frustration effects.[27−29] Notable homovalent clusters include $\{Mn^{II}_7\}$ and $\{Mn^{II}_{19}\}$ species that bear structural similarities to the layered $Mn(OH)_2$ pyrochroite mineral.[17−20,30] Indeed, the reported $\{Mn^{II}_7\}$ clusters exhibit spin frustration, and the $\{Mn^{II}_{19}\}$ clusters exhibit antiferromagnetic spin correlations. Additionally, the one-dimensional solid $\{Mn_4Cl_8(THF)_6(Mn(THF)_2Cl_2\}_\infty$ contains tetranuclear Mn^{II} clusters, and all spin centers in the material engage in antiferromagnetic coupling.[31] The present templating approach therefore offers a powerful new opportunity to study magnetic frustration and underlying coupling interactions as well as potential confinement effects in a technologically relevant material.

EXPERIMENTAL SECTION

General Information. All manipulations were performed using standard Schlenk techniques or in a nitrogen-atmosphere VAC glovebox. Acetonitrile (MeCN) and toluene were dried using a commercial solvent purification system designed by JC Meyer Solvent Systems and stored over 3 Å molecular sieves prior to use. Compound **1** was prepared as previously reported.[32] All other compounds were purchased and used as received. Metal content analysis via inductively coupled plasma optical emission spectrometry (ICP-OES) was conducted as previously reported.[22]

Synthesis of 1(MnBr$_2$)$_{14}$ (CCDC 2070582). Stoichiometric reactions were performed using microcrystalline powder samples of **1** in the presence of single crystals that were later characterized by crystallography. Single crystals of **1** (<0.1 mg) suspended in toluene were transferred into a thick-walled borosilicate tube. Most of the solvent was decanted, followed by the addition of microcrystalline **1** (100 mg), 19 equiv of $MnBr_2$ (191.7 mg, 0.8927 mmol), and 3.0 mL of 5% (v/v) MeCN in toluene. The reaction mixture was degassed by three freeze−pump−thaw cycles, after which the tube was flame-sealed and then placed in an oven preheated to 120 °C. The mixture was allowed to react for 1 month at this temperature, resulting in a color change from white to yellow for both the crystals and the powder. Most of the solution was removed by pipet, and the crystals were subsequently soaked in 3 mL of fresh 5% (v/v) MeCN in toluene at 32 °C for 24 h. The supernatant was subsequently decanted, and this soaking procedure was repeated two more times. Unreacted $MnBr_2$ solid powder was removed by careful transfer of the framework crystals and microcrystals into a new vial prior to each wash. A slurry containing most of the microcrystalline powder was separated from the crystals and pipetted into a new vial, after which the solvent was removed under reduced pressure at 80 °C to give a microcrystalline powder sample of **1**(MnBr$_2$)$_{14}$. The remaining single crystals were then used for single-crystal X-ray diffraction experiments. Anal. Calcd for $C_{84}H_{54}Br_{28}Mn_{14}N_{18}O_{32}Zr_6$: C, 18.75; H, 1.01; N, 4.69. Found: C, 20.90; H, 1.55; N, 3.91.

Single-Crystal X-ray Diffraction. X-ray diffraction analysis was performed on a single crystal coated with Paratone-N oil and mounted on a MiTeGen loop. The crystal was frozen at 100 K by an Oxford Cryosystems Cryostream 700 Plus. Data were collected at Beamline 11.3.1 at the Advanced Light Source, Lawrence Berkeley National Laboratory, using synchrotron radiation (λ = 0.7288 Å) on a Bruker D8 diffractometer equipped with a Bruker PHOTON100 CMOS detector. Raw data were integrated and corrected for Lorentz and polarization effects using Bruker AXS *SAINT* software.[33] Absorption corrections were applied using *SADABS*.[34] The structure was solved using direct methods with *SHELXS*[35,36] and refined using *SHELXL*[37] operated in the *OLEX2*[38] interface. No significant crystal decay was observed during data collection.

Structural refinement proceeded analogously to previous work.[32] Voids in the structures that result from disordered solvent that could not be modeled, large anisotropic displacement parameters that result from linker and solvent disorder, and low data resolution gave rise to A and B level alerts from checkCIF. Responses addressing these alerts have been included in the CIF and can be read in the report generated by checkCIF. Modeling the unassigned electron density using *SQUEEZE*,[39] as implemented in the *PLATON*[40] interface, results in an artificially inflated linker occupancy. Consequently, refinement prior to the implementation of *SQUEEZE* is reported.

Powder X-ray Diffraction. A microcrystalline powder sample of **1**(MnBr$_2$)$_{14}$ was loaded into a 1.0 mm boron-rich glass capillary inside a nitrogen-atmosphere glovebox, and the capillary was flame-sealed. The capillary was placed onto a zero-background plate of a Bruker D8 Advance diffractometer and collected using a Cu Kα (λ = 1.5406 Å) X-ray source, scanning 2θ between 3 and 50° at a scan rate of 0.2 s step^{-1} with a step size of 0.02°.

Electron Microscopy. Scanning electron microscopy (SEM) was performed using a FEI Quanta Dual Beam FIB 0.5−30 kV microscope operating at 10 kV at the Biomolecular Nanotechnology Center, University of California—Berkeley. Energy-dispersive X-ray spectroscopy (EDS) maps were obtained at room temperature using an Oxford EDS detector attached to the SEM microscope.

SQUID Magnetometry. Sample preparation proceeded as previously reported.[22] Magnetic susceptibility measurements were performed using a Quantum Design MPMS2-XL SQUID magnetometer. Direct-current (dc) magnetic susceptibility measurements were collected in the temperature range 2−300 K under applied magnetic fields of 0.01, 0.1, and 1 T. Magnetic hysteresis measurements were performed at a sweep rate of 2.4 mT s^{-1}. Diamagnetic corrections were applied to the data using Pascal's constants to give χ_D = −0.00202172 emu mol^{-1} [**1**(MnBr$_2$)$_{14}$] and χ_D = −0.00024306 emu mol^{-1} (eicosane).

COMPUTATIONAL DETAILS

Density Functional Theory (DFT) Calculations. All DFT calculations were performed using the *Gaussian G16.A3* software suite.[41] The Minnesota M11L meta-GGA functional was used in conjunction with an ultrafine integration grid.[42] A split-basis-set construct was used, with all Mn atoms treated with the Dunning triple-ζ cc-pVTZ, all Br and N atoms treated with the double-ζ cc-pVDZ, and all C, O, and H atoms treated with the Pople 6-31G basis set.[43,44] The crystal geometry was examined via single-point, broken-symmetry calculations with only the bipyridine linkers, MeCN groups, and $Mn_{19}Br_{36}$ magnetic sheet included. The structure was treated as a 2+ cation, with the central Mn ion holding the excess charge. A total of 31 fragments were constructed: 1 central Mn^{2+} ion, 18 $MnBr_2$ groups, 6 bipyridine ligands, and 6 MeCN groups. Attempts to simulate the magnetic data for the cluster with PHI proved impossible because of the memory requirements for a system with 19 $S = {}^5/_2$ ions.

Broken-symmetry calculations were carried out on 18 representative magnetic configurations to determine the values of $\langle S^2 \rangle$ and the energy for each. The Minnesota functional M11L was used with the basis sets cc-pVTZ (Mn), cc-pVDZ (Br and N), and 6-31G (C, O, and H). The M11L functional was selected because it is benchmarked to work well with transition metals and was found to be the most computationally efficient for this system among a series of functionals including M062X, PBE, and B3LYP. Because B3LYP is a common functional for *J*-constant estimation, we include a subset of calculations with B3LYP to demonstrate the correspondence between the two functionals (Tables S3 and S6).

Monte Carlo Simulations. In order to obtain the magnetic susceptibility and hysteresis curves from the calculated magnetic exchange coupling constants, we performed Monte Carlo simulations using the Metropolis algorithm.[45] For each simulation, 1000 clusters (14000 Mn^{II} centers) comprised of the cluster sizes Mn_6, Mn_{12}, Mn_{18}, and Mn_{19} were constructed such that the average cluster size is Mn_{14}. We attempt a spin flip of each Mn^{II} center within each cluster for a total of 14000 attempted spin flips for each ensemble and iterated this process over 10000 Monte Carlo steps. This ensured that the calculated magnetization for each Monte Carlo step was representative of a system with an average Mn population of 14. The first 2000 Monte Carlo steps were excluded in the calculation of averages so that each system was able to reach equilibrium.

https://doi.org/10.1021/acs.inorgchem.1c01345
Inorg. Chem. 2021, 60, 16103−16110

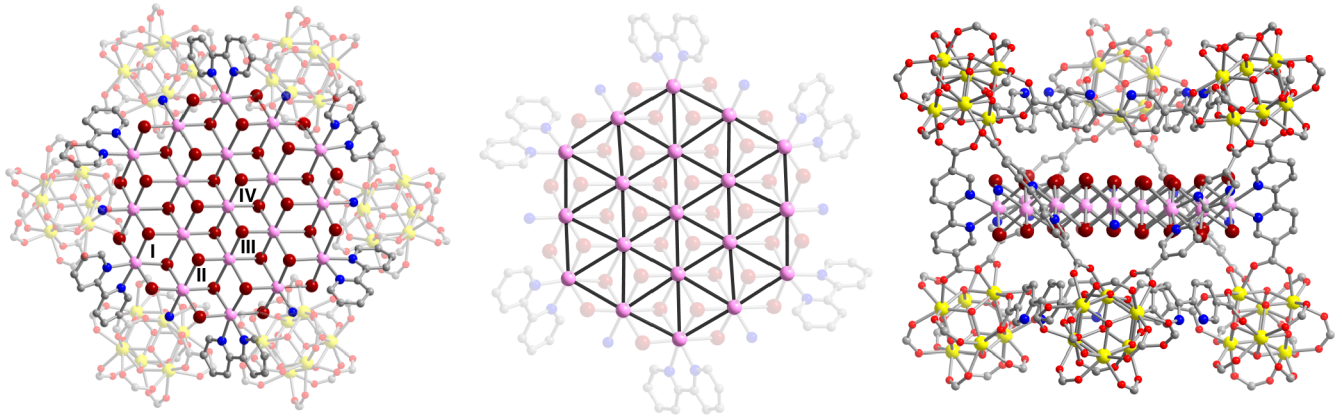

Figure 1. Portions of the crystal structure of $\mathbf{1}(MnBr_2)_{11}$ at 100 K as determined from single-crystal X-ray diffraction. (Left) Top-down view of the templated cluster, which features 19 Mn^{II} ions arranged in a triangular lattice. The four crystallographically distinct Mn^{II} sites are labeled with roman numerals. (Middle) Cluster view highlighting the triangular lattice of Mn atoms. (Right) Cluster side view. Yellow, pink, dark-red, red, blue, and gray spheres represent Zr, Mn, Br, O, N, and C atoms, respectively; H atoms and outer-sphere Br anions are omitted for clarity.

RESULTS AND DISCUSSION

Synthesis and Structural Characterization. The treatment of single crystals of **1** with 19 equiv of $MnBr_2$ in a 1:10 (v/v) mixture of MeCN and toluene affords $\mathbf{1}(MnBr_2)_{11}$. Single-crystal X-ray diffraction characterization revealed a structure containing 19 total Mn positions arranged in a triangular lattice to afford 24 triangular circuits (Figure 1). While the triangular circuits are not themselves equilateral, the crystal structure space group symmetry of $Pa\bar{3}$ enforces a local D_{3d} point group symmetry for the cluster. A total of 4 of the 19 Mn positions are crystallographically distinct. Sites I and II each generate six symmetrically equivalent positions that together comprise the outer ring of the cluster. Site I is bound to the bipyridine moiety of the framework, and site II bridges adjacent site I positions. Site III consists of six equivalent positions that comprise the inner ring of the cluster, and site IV is the central Mn^{II} ion. The site occupancies are highest at the cluster edges and decrease toward the center, with values of 0.864(12), 0.625(12), 0.382(12), and 0.25(3) for sites I–IV, respectively. Close examination of the crystal structure reveals that site II adopts a pseudooctahedral $MnBr_5(MeCN)$ coordination environment, but it is only possible to resolve the N atom of the MeCN ligand. At full occupancy, the cluster can therefore be described as the divalent cation $Mn_{19}Br_{36}(bpydc)_6(MeCN)_6^{2+}$ with two additional outer-sphere Br anions (Figure S1). Fractional site occupancies, however, indicate a mixture of cluster sizes, with no more than 25(3)% of the framework pores in $\mathbf{1}(MnBr_2)_{11}$ bearing a fully populated Mn_{19} cluster.

Treatment of microcrystalline **1** with 19 equiv of $MnBr_2$ under synthetic conditions identical with those used for the single crystals afforded $\mathbf{1}(MnBr_2)_{14}$ with a higher overall metal occupancy [73.3(2)%], as determined using ICP-OES. The higher overall metal occupancy suggests a greater fraction of fully populated Mn_{19} clusters; however, we still expect a mixture of cluster sizes in line with the single-crystal X-ray diffraction experiments. Further characterization of $\mathbf{1}(MnBr_2)_{14}$ by powder X-ray diffraction (Figure S2) as well as SEM and EDS (Figures S3 and S4) confirmed the sample purity and uniform incorporation of $MnBr_2$. The smaller particle sizes of microcrystalline **1** may facilitate the increased metal loading relative to that determined for the single crystals. The use of more than 19 equiv of $MnBr_2$ did not increase the metal loading achievable in single-crystalline or microcrystalline **1**.

At full occupancy, the $Mn_{19}Br_{36}$ cluster corresponds to a fragment excised from a single layer of the bulk $MnBr_2$ solid-state structure. The average nearest-neighbor Mn···Mn distance in the cluster is 3.74(6) Å, which is slightly compressed relative to that in the bulk material (3.922 Å).[23] The rigidity of the framework likely enforces the compressed cluster geometry, despite the ability of the framework linkers to accommodate minor strain. The Mn–Br–Mn bond angles of the cluster range from 87.2(2) to 92.8(2)°, compared with 90° in the bulk material. Bulk $MnBr_2$ adopts an antiferromagnetically ordered state below 2.16 K, wherein each $MnBr_2$ layer consists of two-metal-atom-wide ferromagnetic stripes with antiferromagnetic coupling between neighboring stripes. Further antiferromagnetic order exists between layers.[23,46,47] However, this spin texture does not necessarily translate into a discrete cluster. In the bulk material, there are several competing exchange mechanisms between nearest neighbors, including antiferromagnetic direct exchange as well as ferromagnetic and antiferromagnetic superexchange.[48,49] Manganese dihalides have also been shown to exhibit significant coupling between second-nearest and even third-nearest neighbors.[50] Consequently, the ground-state magnetic structure for a finite-sized $MnBr_2$ cluster will be highly sensitive to Mn···Mn distances and Mn–Br–Mn bond angles.

Investigation of the Magnetic Properties by SQUID Magnetometry. dc magnetic susceptibility data were collected to probe the magnetic interactions present in microcrystalline $\mathbf{1}(MnBr_2)_{14}$ (Figure 2a). At 300 K, the product of the molar magnetic susceptibility and temperature ($\chi_M T$) is 59.4 emu K mol^{-1}, which corresponds well to the expected value for 14 uncoupled, high-spin Mn^{II} ions (61.25 emu K mol^{-1} assuming g = 2.00). The magnitude of $\chi_M T$ continuously decreases as the temperature is lowered, indicative of antiferromagnetic coupling between Mn centers. This conclusion is further supported by the negative Weiss temperature of −27.2 K determined from a Curie–Weiss fit to $1/\chi_M$ collected under a 0.01 T field (Figure S5). Variable-field magnetization data collected at 2 K feature minimal curvature, and at the highest field of 7 T, M reaches a value of only 30.9 μ_B (Figure 2b). This value is approximately half that expected for parallel alignment of all Mn spins (70 μ_B), again supporting

https://doi.org/10.1021/acs.inorgchem.1c01345
Inorg. Chem. 2021, 60, 16103–16110

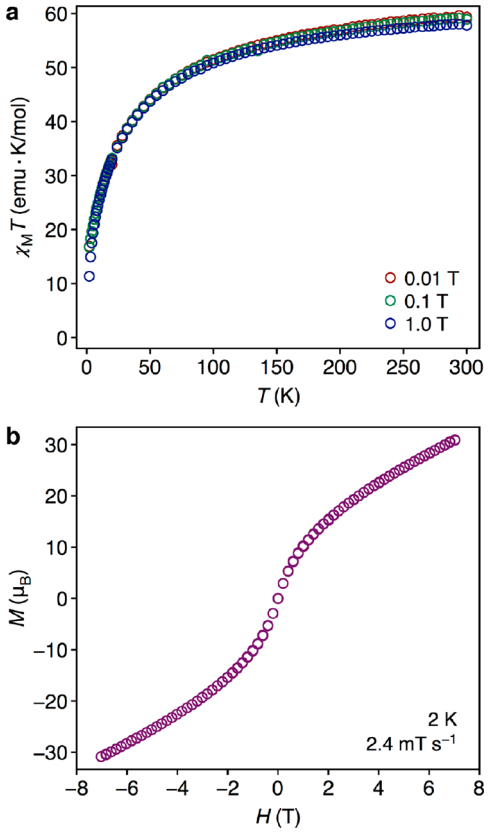

Figure 2. (a) Plot of $\chi_M T$ versus T data for $\mathbf{1}(MnBr_2)_{14}$ under applied fields of 0.01, 0.1, and 1.0 T. (b) Magnetization versus applied field data for $\mathbf{1}(MnBr_2)_{14}$ collected at 2 K using a sweep rate of 2.4 mT s^{-1}.

the presence of antiferromagnetic coupling between Mn^{II} centers. While a detailed interpretation of the experimental magnetic data is complicated by the mixture of cluster sizes present in $\mathbf{1}(MnBr_2)_{14}$, a structurally related $\{Mn_{19}(OH)_{12}\}^{26+}$ cluster exhibits similar magnetic susceptibility and magnetization behavior. In the $\{Mn_{19}(OH)_{12}\}^{26+}$ cluster, the lack of a round maximum in the magnetic susceptibility data and the nonlinearity of the magnetization data are attributed to a near-continuous spread of antiferromagnetic J constants.[20] In our system, J constants likely vary within a specific cluster but will also be affected by the variable Mn population. We can therefore conclude that antiferromagnetic interactions are indeed dominant throughout the ensemble but cannot attribute the overall behavior to a specific cluster size.

In tandem with a triangular cluster lattice, these dominant antiferromagnetic interactions are expected to give rise to geometric spin frustration. Multiple weak coupling interactions between Mn^{II} centers, however, are likely to give rise to many low-lying excited states that further complicate experimental validation of the total ground-state spin (S_{Total}).[27,51] In some situations, collecting reduced magnetization data at low applied fields and temperatures has been shown to mitigate this difficulty.[14,52] In this case, however, we were unable to obtain satisfactory fits to reduced magnetization data collected for microcrystalline $\mathbf{1}(MnBr_2)_{14}$ under fields ranging from 0.1 to 2.0 T and temperatures from 2.0 to 10 K (Figure S6), likely because of the presence of multiple species.

Alternating-current (ac) magnetic susceptibility data collected under zero applied field can offer insight into the ground-state spin population and magnitude because the absence of an applied field mitigates the approach or crossing of excited states with the ground state.[52] In particular, the product of the in-phase molar magnetic susceptibility and temperature ($\chi_M' T$) will be temperature-independent if the ground state is exclusively populated, whereas this product will be temperature-dependent if there is also excited-state population. ac susceptibility data were collected for $\mathbf{1}(MnBr_2)_{14}$ between 2 and 10 K using a 4 Oe field oscillating at frequencies from 1 to 500 Hz (Figures S7 and S8). No out-of-phase signal (χ_M'') is detected, but the corresponding plot of $\chi_M' T$ versus T is clearly temperature-dependent (Figure S9). This result suggests the presence of a subset of cluster sizes with low-lying excited states. Similar behavior attributable to low-lying excited states was reported for disklike Mn^{II}_7 clusters.[17,18] Despite the variable Mn population in our system, experimental magnetic characterization of $\mathbf{1}(MnBr_2)_{14}$ is therefore broadly consistent with planar, antiferromagnetically coupled Mn^{II} clusters that display spin frustration.

Exchange Coupling Constants. From a theoretical perspective, we are most interested in understanding the magnetic properties of a fully populated Mn_{19} cluster in order to guide future research efforts. To probe the magnetic interactions and ground-state structure of this particular species further, we turned to computational methods. A $Mn_{19}Br_{36}$ cluster model was constructed using atomic coordinates from the single-crystal structure of $\mathbf{1}(MnBr_2)_{11}$, including bipyridine and MeCN ligands but excluding the zirconium framework nodes and the two outer-sphere bromide anions. The structure was treated as a 2+ cation, with the central Mn^{II} ion holding the excess charge to maintain symmetry. Together, these elements preserve the essential features of $\mathbf{1}(MnBr_2)_{11}$. We then constructed 18 representative magnetic configurations (Figures S10–S27) and determined the energy (E) and total spin magnitude ($\langle S_{Total}^2 \rangle$) for each configuration using DFT calculations performed with the Minnesota M11L meta-GGA functional.[53] By examining the spin flips and associated energy differences between pairs of magnetic configurations, we deduced nine significant coupling interactions, namely, between adjacent metal ions and between the central metal ion and outer ring of 12 metal ions (see the Supporting Information for details).

We then employed the Yamaguchi generalized spin-projection method for multispin systems[54] to first isolate all nine antiferromagnetic spin-correlation functions $^{AF}\langle S_i \cdot S_j \rangle$ via the solution to a series of 10 linear equations for $\langle S_{Total}^2 \rangle$ (Table S5). The correlation functions determined in this way were all found to differ by less than 0.1% from the value of $-|S_i| \cdot |S_j|$ (here -6.25 for $S_{Mn} = {}^5/_2$), which indicates virtually no orbital overlap between Mn^{II} centers. This is unsurprising, given the average distance of ~3.74 Å between adjacent metal sites, and permits us to use a simple Ising model to calculate the J constants.[54,55] Using $-|S_i| \cdot |S_j|$ for our spin-correlation functions, we then constructed a series of 18 linear equations of the form

$$E = E_0 - 2 \sum_{\alpha} J_\alpha \sum_{i,j} \langle S_i \cdot S_j \rangle \quad (1)$$

where E is the energy for a particular magnetic configuration determined by DFT, J_α sums over the nine coupling constants, and $S_i \cdot S_j$ sums over the six pairs of Mn^{II} centers associated with each J.[54] Using these equations, we fit nine different J values and a value for E_0. A comparison of the DFT energies with those output by eq 1 and calculated J constants (Table S6 and

https://doi.org/10.1021/acs.inorgchem.1c01345
Inorg. Chem. 2021, 60, 16103−16110

Figure S28) indicates the strength of this nine-J model for the magnetic interactions of the cluster. All interactions are found to be antiferromagnetic with the strongest interactions toward the center of the cluster (Figure 3).

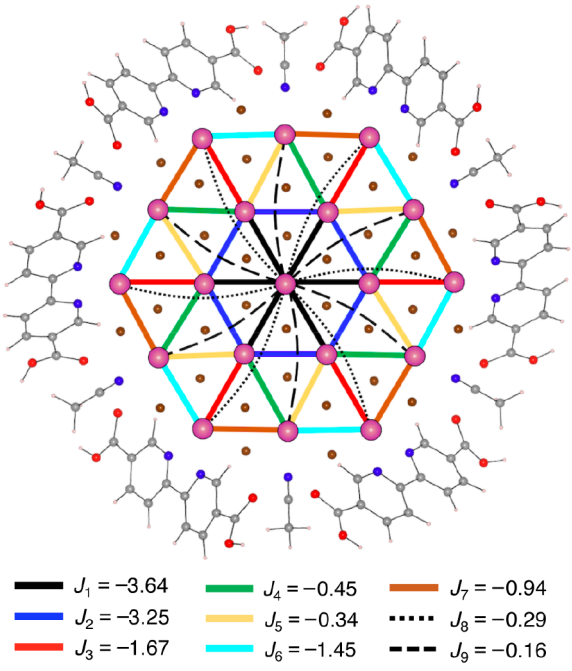

Figure 3. Illustration of the nine significant magnetic exchange pathways determined for the $Mn_{19}Br_{36}$ cluster model. Magnetic interactions between adjacent ions are indicated with solid-colored lines, while interactions between the central ion and the outer ring of 12 ions are represented by dashed and dotted lines. All J values are in reciprocal centimeters.

Monte Carlo Simulations. Before calculating the energies of the potential magnetic configurations for the Mn_{19} cluster, we assess the validity of the calculated J constants. We therefore employ Monte Carlo simluations to compare the experimental magnetic susceptibility and hysteresis data with those obtained from the parameters calculated above. Experimental magnetic data tests were performed on $\mathbf{1}(MnBr_2)_{14}$, which likely consists of a mixture of clusters. To simplify Monte Carlo simulations, we consider a subset of four potential cluster sizes. Namely, we consider clusters constructed from site I (Mn_6), sites I and II (Mn_{12}), sites I–III (Mn_{18}), and sites I–IV (Mn_{19}). To further simplify calculations, we assume that the J constants calculated by DFT for Mn_{19} will be the same for Mn_{18}, excluding those J constants involving site IV. For Mn_{12}, we use the methodology described above to determine values for J_6' and J_7' that relate sites I and II. We find these values to be −1.69 and −1.44 cm^{-1}, respectively. For Mn_6, we assume no coupling between Mn centers. For Monte Carlo simulations, an ensemble of 1000 clusters is randomly constructed such that the average Mn population per cluster is 14, as in $\mathbf{1}(MnBr_2)_{14}$. A spin flip is attempted on each of the 14000 Mn^{II} ions within the ensemble for each Monte Carlo step, and this process is iterated over 10000 steps. The line shape and magnitude of the resulting magnetic susceptibility and hysteresis curves (Figures S29 and S30) correspond well with the experimental data and confirm the applicability of the calculated J constants.

Spin Configurations. Using these J constants, it is then possible to use eq 1 to reliably predict the Ising energy of any spin configuration for a Mn_{19} cluster without additional DFT calculations. With 19 Mn centers in the core of the cluster, there are hundreds of thousands of possible spin configurations. We fixed the central ion as "spin up", iterated through all 2^{18} different spin configurations, and calculated the Ising energy of each configuration relative to the Ising energy of the high-spin state. The resulting pairs of spin and energy were further reduced by eliminating all repeated instances of combined spin and energy to afford 9500 distinct combinations (Figure S31). The resulting energy-level diagram, a portion of which is shown in Figure 4a, reveals numerous low-

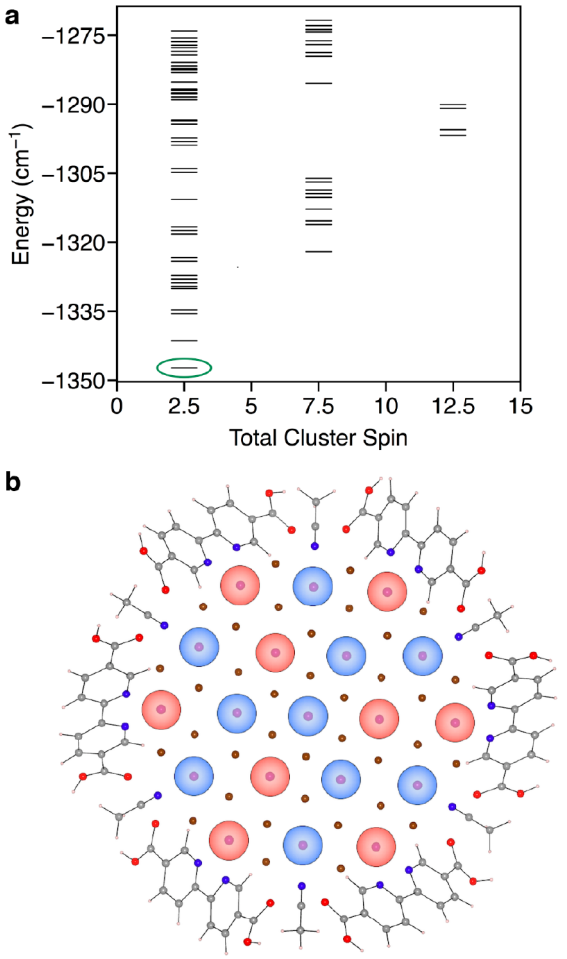

Figure 4. (a) Subset of the Ising energy levels within 75 cm^{-1} of the ground state, as computed using eq 1. Energy levels were adjusted so the high-spin state of $S_{Total} = {}^{95}/_{2}$ is at 0 cm^{-1}. The ground state is indicated by a green ellipse. (b) Ground-state magnetic configuration. Ions shaded in blue correspond to spin up. Ions shaded in red correspond to spin down.

lying excited-state configurations that are consistent with the temperature dependence of the ac magnetic susceptibility data. Finally, we identified a doubly degenerate, highly geometrically frustrated ground-state configuration with a total spin of $S_{Total} = {}^{5}/_{2}$ (Figure 4b). Overall, there are 18 pairs of frustrated interactions in the ground state: three between the central ion and the ions of the middle ring, six between the central ion and ions of the outer ring, and nine between the middle and outer rings of ions.

https://doi.org/10.1021/acs.inorgchem.1c01345
Inorg. Chem. 2021, 60, 16103−16110

CONCLUSIONS

The foregoing results illustrate the utility of metal−organic frameworks as ligand templates to target clusters with specific structures and properties. Using **1**, we were able to template and confine the growth of a rare two-dimensional, homovalent Mn^{II} cluster that also exhibits spin frustration. Calculations performed for a representative $Mn_{19}Br_{36}^{2+}$ cluster fragment predict a ground-state magnetic configuration that is notably distinct from the striped antiferromagnetic phase of bulk $MnBr_2$. This result further suggests that isolating monolayers of $MnBr_2$ may be an interesting research direction and that its magnetic properties could be affected by modulating the lattice and exchange parameters.

ASSOCIATED CONTENT

Supporting Information

The Supporting Information is available free of charge at https://pubs.acs.org/doi/10.1021/acs.inorgchem.1c01345.

Additional experimental and computational details, powder X-ray diffraction data, single-crystal X-ray diffraction data, magnetic susceptibility data, electron microscopy data, and additional references (PDF)

Accession Codes

CCDC 2070582 contains the supplementary crystallographic data for this paper. These data can be obtained free of charge via www.ccdc.cam.ac.uk/data_request/cif, or by emailing data_request@ccdc.cam.ac.uk, or by contacting The Cambridge Crystallographic Data Centre, 12 Union Road, Cambridge CB2 1EZ, UK; fax: +44 1223 336033.

AUTHOR INFORMATION

Corresponding Author

Jeffrey R. Long − *Department of Chemistry and Department of Chemical and Biomolecular Engineering, University of California—Berkeley, Berkeley, California 94720, United States; Materials Sciences Division, Lawrence Berkeley National Laboratory, Berkeley, California 94720, United States;* orcid.org/0000-0002-5324-1321; Email: jrlong@berkeley.edu

Authors

Ari Turkiewicz − *Department of Chemistry, University of California—Berkeley, Berkeley, California 94720, United States;* orcid.org/0000-0001-5729-0289

Warren Tomlinson − *Department of Physics, Naval Postgraduate School, Monterey, California 93943, United States*

Miguel I. Gonzalez − *Department of Chemistry, University of California—Berkeley, Berkeley, California 94720, United States;* Present Address: Department of Chemistry and Chemical Biology, Harvard University, 12 Oxford Street, Cambridge, Massachusetts 02138, United States

Joseph P. Hooper − *Department of Physics, Naval Postgraduate School, Monterey, California 93943, United States;* orcid.org/0000-0003-4899-1934

Complete contact information is available at: https://pubs.acs.org/10.1021/acs.inorgchem.1c01345

Notes

The authors declare no competing financial interest.

ACKNOWLEDGMENTS

This research was supported through a Multidisciplinary University Research Initiatives Program funded by the U.S. Department of Defense, Office of Naval Research, under Award N00014-15-1-2681. Single-crystal X-ray diffraction experiments were performed at Beamline 11.3.1 at the Advanced Light Source, Lawrence Berkeley National Laboratory. The Advanced Light Source is supported by the Director, Office of Science, Office of Basic Energy Sciences, U.S. Department of Energy, under Contract DE-AC02-05CH11231. We thank the U.S. National Science Foundation for providing graduate fellowship support for A.T. In addition, we thank Dr. Simon J. Teat for experimental assistance and helpful discussions and Dr. Katie R. Meihaus for editorial assistance.

REFERENCES

(1) Schnack, J. Effects of Frustration on Magnetic Molecules: A Survey from Oliver Kahn Until Today. *Dalton Trans.* **2010**, *39*, 4677−4686.

(2) Ghirri, A.; Van Tol, J.; Vitorica-Yrezabal, I.; Timco, G. A.; Winpenny, R. E. P. Effects of the Dzyaloshinskii-Moriya Interaction in Cr_3 Triangular Spin Clusters Detected by Specific Heat and Multi-Frequency Electron Spin Resonance. *Dalton Trans.* **2015**, *44*, 14027−14033.

(3) Troiani, F.; Stepanenko, D.; Loss, D. Hyperfine-Induced Decoherence in Triangular Spin-Cluster Qubits. *Phys. Rev. B: Condens. Matter Mater. Phys.* **2012**, *86*, 161409.

(4) Waldmann, O.; Stamatatos, T. C.; Christou, G.; Güdel, H. U.; Sheikin, I.; Mutka, H. Quantum Phase Interference and Néel-Vector Tunneling in Antiferromagnetic Molecular Wheels. *Phys. Rev. Lett.* **2009**, *102*, 18−22.

(5) Baker, M. L.; Guidi, T.; Carretta, S.; Ollivier, J.; Mutka, H.; Güdel, H. U.; Timco, G. A.; Mcinnes, E. J. L.; Amoretti, G.; Winpenny, R. E. P.; Santini, P. Spin Dynamics of Molecular Nanomagnets Unravelled at Atomic Scale by Four-Dimensional Inelastic Neutron Scattering. *Nat. Phys.* **2012**, *8*, 906−911.

(6) Yamashita, M.; Nakata, N.; Senshu, Y.; Nagata, M.; Yamamoto, H. M.; Kato, R.; Shibauchi, T.; Matsuda, Y. Highly Mobile Gapless Excitations in a Two-Dimensional Candidate Quantum Spin Liquid. *Science* **2010**, *328*, 1246−1248.

(7) Shores, M. P.; Nytko, E. A.; Bartlett, B. M.; Nocera, D. G. A Structurally Perfect S = 1/2 Kagomé Antiferromagnet. *J. Am. Chem. Soc.* **2005**, *127*, 13462−13463.

(8) Banerjee, A.; Bridges, C. A.; Yan, J. Q.; Aczel, A. A.; Li, L.; Stone, M. B.; Granroth, G. E.; Lumsden, M. D.; Yiu, Y.; Knolle, J.; Bhattacharjee, S.; Kovrizhin, D. L.; Moessner, R.; Tennant, D. A.; Mandrus, D. G.; Nagler, S. E. Proximate Kitaev Quantum Spin Liquid Behaviour in a Honeycomb Magnet. *Nat. Mater.* **2016**, *15*, 733−740.

(9) Okamoto, Y.; Nohara, M.; Aruga-Katori, H.; Takagi, H. Spin-Liquid State in the S = 1/2 Hyperkagome Antiferromagnet $Na_4Ir_3O_8$. *Phys. Rev. Lett.* **2007**, *99*, 4−7.

(10) Rau, J. G.; Gingras, M. J. P. Frustrated Quantum Rare-Earth Pyrochlores. *Annu. Rev. Condens. Matter Phys.* **2019**, *10*, 357−386.

(11) Woolfson, R. J.; Timco, G. A.; Chiesa, A.; Vitorica-Yrezabal, I. J.; Tuna, F.; Guidi, T.; Pavarini, E.; Santini, P.; Carretta, S.; Winpenny, R. E. P. $[CrF(O_2C^tBu)_2]_9$: Synthesis and Characterization of a Regular Homometallic Ring with an Odd Number of Metal Centers and Electrons. *Angew. Chem., Int. Ed.* **2016**, *55*, 8856−8859.

(12) Blake, A. J.; Gould, R. O.; Grant, C. M.; Milne, P. E. Y.; Parsons, S.; Winpenny, R. E. P. Reactions of Copper Pyridonate Complexes with Hydrated Lanthanoid Nitrates. *J. Chem. Soc., Dalton Trans.* **1997**, 485−495.

(13) Müller, A.; Luban, M.; Schröder, C.; Modler, R.; Kögerler, P.; Axenovich, M.; Schnack, J.; Canfield, P.; Bud'ko, S.; Harrison, N. Classical and Quantum Magnetism in Giant Keplerate Magnetic Molecules. *ChemPhysChem* **2001**, *2*, 517−521.

(14) Stamatatos, T. C.; Foguet-Albiol, D.; Poole, K. M.; Wernsdorfer, W.; Abboud, K. A.; O'Brien, T. A.; Christou, G. Spin Maximization from S = 11 to S = 16 in Mn_7 Disk-like Clusters: Spin Frustration Effects and Their Computational Rationalization. *Inorg. Chem.* **2009**, *48*, 9831−9845.
(15) Deng, Y. K.; Su, H. F.; Xu, J. H.; Wang, W. G.; Kurmoo, M.; Lin, S. C.; Tan, Y. Z.; Jia, J.; Sun, D.; Zheng, L. S. Hierarchical Assembly of a $\{Mn^{II}_{19}Mn^{III}_{4}\}$ Brucite Disc: Step-by-Step Formation and Ferrimagnetism. *J. Am. Chem. Soc.* **2016**, *138*, 1328−1334.
(16) Mukherjee, S.; Bagai, R.; Abboud, K. A.; Christou, G. Raising the Spin of Fe^{III}_{7} Disklike Clusters: The Power of Molecular Spin Frustration. *Inorg. Chem.* **2011**, *50*, 3849−3851.
(17) Vignesh, K. R.; Langley, S. K.; Murray, K. S.; Rajaraman, G. What Controls the Magnetic Exchange Interaction in Mixed- and Homo-Valent Mn_7 Disc-like Clusters? A Theoretical Perspective. *Chem. - Eur. J.* **2015**, *21*, 2881−2892.
(18) Langley, S. K.; Chilton, N. F.; Massi, M.; Moubaraki, B.; Berry, K. J.; Murray, K. S. Synthesis and Characterization of Homo- and Heterovalent Tetra- Hexa- Hepta- and Decanuclear Manganese Clusters Using Pyridyl Functionalized β-Diketone, Carboxylate and Triethanolamine Ligands. *Dalton Trans.* **2010**, *39*, 7236−7249.
(19) Pohl, I. A. M.; Westin, L. G.; Kritikos, M. Preparation, Structure, and Properties of a New Giant Manganese Oxo-Alkoxide Wheel, $[Mn_{19}O_{12}(OC_2H_4OCH_3)_{14}(HOC_2H_4OCH_3)_{10}]\bullet HOC_2H_4OCH_3$. *Chem. - Eur. J.* **2001**, *7*, 3438−3445.
(20) Bassil, B. S.; Ibrahim, M.; Al-Oweini, R.; Asano, M.; Wang, Z.; van Tol, J.; Dalal, N. S.; Choi, K.-Y.; Ngo Biboum, R.; Keita, B.; Nadjo, L.; Kortz, U. A Planar $\{Mn_{19}(OH)_{12}\}^{26+}$ Unit Incorporated in a 60-Tungsto-6-Silicate Polyanion. *Angew. Chem., Int. Ed.* **2011**, *50*, 5961−5964.
(21) Grohol, D.; Matan, K.; Cho, J. H.; Lee, S. H.; Lynn, J. W.; Nocera, D. G.; Lee, Y. S. Spin Chirality on a Two-Dimensional Frustrated Lattice. *Nat. Mater.* **2005**, *4*, 323−328.
(22) Gonzalez, M. I.; Turkiewicz, A. B.; Darago, L. E.; Oktawiec, J.; Bustillo, K.; Grandjean, F.; Long, G. J.; Long, J. R. Confinement of Atomically Defined Metal Halide Sheets in a Metal−Organic Framework. *Nature* **2020**, *577*, 64.
(23) Wollan, E. O.; Koehler, W. C.; Wilkinson, M. K. Neutron Diffraction Study of the Magnetic Properties of $MnBr_2$. *Phys. Rev.* **1958**, *110*, 638−646.
(24) Mounet, N.; Gibertini, M.; Schwaller, P.; Campi, D.; Merkys, A.; Marrazzo, A.; Sohier, T.; Castelli, I. E.; Cepellotti, A.; Pizzi, G.; Marzari, N. Two-Dimensional Materials from High-Throughput Computational Exfoliation of Experimentally Known Compounds. *Nat. Nanotechnol.* **2018**, *13*, 246−252.
(25) Wei, G.; Czaplewski, D. A.; Lenferink, E. J.; Stanev, T. K.; Jung, I. W.; Stern, N. P. Size-tunable Lateral Confinement in Monolayer Semiconductors. *Sci. Rep.* **2017**, *7*, 3324.
(26) De Siena, M. C.; Creutz, S. E.; Regan, A.; Malinowski, P.; Jiang, Q.; Kluherz, K. T.; Zhu, G.; Lin, Z.; De Yoreo, J. J.; Xu, X.; Chu, J.-H.; Gamelin, D. R. Two-Dimensional van der Waals Nanoplatelets with Robust Ferromagnetism. *Nano Lett.* **2020**, *20*, 2100−2106.
(27) Stamatatos, T. C.; Christou, G. Mixed Valency in Polynuclear Mn^{II}/Mn^{III}, Mn^{III}/Mn^{IV} and $Mn^{II}/Mn^{III}/Mn^{IV}$ Clusters: A Foundation for High-Spin Molecules and Single-Molecule Magnets. *Philos. Trans. R. Soc., A* **2008**, *366*, 113−125.
(28) Sañudo, E. C.; Cauchy, T.; Ruiz, E.; Laye, R. H.; Roubeau, O.; Teat, S. J.; Aromí, G. Molecules Composed of Two Weakly Magnetically Coupled $[Mn^{III}_{4}]$ Clusters. *Inorg. Chem.* **2007**, *46*, 9045−9047.
(29) Ako, A. M.; Hewitt, I. J.; Mereacre, V.; Clérac, R.; Wernsdorfer, W.; Anson, C. E.; Powell, A. K. A Ferromagnetically Coupled Mn_{19} Aggregate with a Record *S* = 83/2 Ground Spin State. *Angew. Chem., Int. Ed.* **2006**, *45*, 4926−4929.
(30) Christensen, A. N.; Ollivier, G. Hydrothermal Preparation and Low Temperature Magnetic Properties of $Mn(OH)_2$. *Solid State Commun.* **1972**, *10*, 609−614.
(31) Zhao, H.; Clérac, R.; Sun, J. S.; Ouyang, X.; Dunbar, K. R.; Clemente-Juan, J. M.; Gómez-García, C. J.; Coronado, E. A Comparative Structural and Magnetic Study of Three Compounds Based on the Cluster Unit $M_4Cl_8(THF)_6$ (M = Mn, Fe, Co). *J. Solid State Chem.* **2001**, *159*, 281−292.
(32) Gonzalez, M. I.; Bloch, E. D.; Mason, J. A.; Teat, S. J.; Long, J. R. Single-crystal-to-single-crystal metalation of a metal-organic framework: a route toward structurally well-defined catalysts. *Inorg. Chem.* **2015**, *54*, 2995−3005.
(33) *SAINT and APEX 2 Software for CCD Diffractometers*; Bruker Analytical X-ray Systems, 2000.
(34) Sheldrick, G. M. *SADABS*; Bruker Analytical X-ray Systems, 2014.
(35) Sheldrick, G. M. *SHELXS*; Universität Göttingen, 2014.
(36) Sheldrick, G. M. A short history of SHELX. *Acta Crystallogr., Sect. A: Found. Crystallogr.* **2008**, *A64*, 112−122.
(37) Sheldrick, G. M. *SHELXL*; Universität Göttingen, 2014.
(38) Dolomanov, O. V.; Bourhis, L. J.; Gildea, R. J.; Howard, J. A. K.; Puschmann, H. OLEX2: a complete structure solution, refinement and analysis program. *J. Appl. Crystallogr.* **2009**, *42*, 339−341.
(39) Spek, A. L. PLATON SQUEEZE: a tool for the calculation of the disordered solvent contribution to the calculated structure factors. *Acta Crystallogr., Sect. C: Struct. Chem.* **2015**, *C71*, 9−18.
(40) Spek, A. L. Single-crystal structure validation with the program PLATON. *J. Appl. Crystallogr.* **2003**, *36*, 7−13.
(41) Frisch, M. J.; Trucks, G. W.; Schlegel, H. B.; Scuseria, G. E.; Robb, M. A.; Cheeseman, J. R.; Scalmani, G.; Barone, V.; Petersson, G. A.; Nakatsuji, H.; Li, X.; Caricato, M.; Marenich, A. V.; Bloino, J.; Janesko, B. G.; Gomperts, R.; Mennucci, B.; Hratchian, H. P.; Ortiz, J. V.; Izmaylov, A. F.; Sonnenberg, J. L.; Williams-Young, D.; Ding, F.; Lipparini, F.; Egidi, F.; Goings, J.; Peng, B.; Petrone, A.; Henderson, T.; Ranasinghe, D.; Zakrzewski, V. G.; Gao, J.; Rega, N.; Zheng, G.; Liang, W.; Hada, M.; Ehara, M.; Toyota, K.; Fukuda, R.; Hasegawa, J.; Ishida, M.; Nakajima, T.; Honda, Y.; Kitao, O.; Nakai, H.; Vreven, T.; Throssell, K.; Montgomery, J. A., Jr.; Peralta, J. E.; Ogliaro, F.; Bearpark, M. J.; Heyd, J. J.; Brothers, E. N.; Kudin, K. N.; Staroverov, V. N.; Keith, T. A.; Kobayashi, R.; Normand, J.; Raghavachari, K.; Rendell, A. P.; Burant, J. C.; Iyengar, S. S.; Tomasi, J.; Cossi, M.; Millam, J. M.; Klene, M.; Adamo, C.; Cammi, R.; Ochterski, J. W.; Martin, R. L.; Morokuma, K.; Farkas, O.; Foresman, J. B.; Fox, D. J. *Gaussian 16*, revision A.03; Gaussian, Inc., 2016.
(42) Peverati, R.; Truhlar, D. G. M11-L: A Local Density Functional That Provides Improved Accuracy for Electronic Structure Calculations in Chemistry and Physics. *J. Phys. Chem. Lett.* **2012**, *3*, 117−124.
(43) Rassolov, V. A.; Ratner, M. A.; Pople, J. A.; Redfern, P. C.; Curtiss, L. A. 6-31G* Basis Set for Third-Row Atoms. *J. Comput. Chem.* **2001**, *22*, 976−984.
(44) Wilson, A. K.; Van Mourik, T.; Dunning, T. H., Jr. Gaussian Basis Sets for use in Correlated Molecular Calculations. VI. Sextuple zeta correlation consistent basis sets for boron through neon. *J. Mol. Struct.: THEOCHEM* **1996**, *388*, 339−349.
(45) Metropolis, N.; Rosenbluth, A.; Rosenbluth, M.; Teller, A.; Teller, E. Equation of State Calculations by Fast Computing Machines. *J. Chem. Phys.* **1953**, *21*, 1087−1092.
(46) Sato, T.; Kadowaki, H.; Masuda, H.; Iio, K. Neutron Diffraction Study of Successive Phase Transitions in the Heisenberg Antiferromagnet $MnBr_2$. *J. Phys. Soc. Jpn.* **1994**, *63*, 4583−4596.
(47) McGuire, M. A. Crystal and Magnetic Structures in Layered, Transition Metal Dihalides and Trihalides. *Crystals* **2017**, *7*, 121.
(48) Goodenough, J. B. *Magnetism and the Chemical Bond*; Interscience Publishers: New York, 1963.
(49) Kanamori, J. Superexchange Interaction and Symmetry Properties of Electron Orbitals. *J. Phys. Chem. Solids* **1959**, *10*, 87−98.
(50) Wiesler, D. G.; Suzuki, M.; Suzuki, I. S.; Rosov, N. Determination of Anomalous Superexchange in $MnCl_2$ and Its Graphite Intercalation Compound. *Phys. Rev. Lett.* **1995**, *75*, 942−945.
(51) Kahn, O. *Molecular Magnetism*; VCH Publishers: New York, 1993.

https://doi.org/10.1021/acs.inorgchem.1c01345
Inorg. Chem. 2021, 60, 16103−16110

(52) Murugesu, M.; Takahashi, S.; Wilson, A.; Abboud, K. A.; Wernsdorfer, W.; Hill, S.; Christou, G. Large Mn_{25} Single-Molecule Magnet with Spin S = 51/2: Magnetic and High-Frequency Electron Paramagnetic Resonance Spectroscopic Characterization of a Giant Spin State. *Inorg. Chem.* **2008**, *47*, 9459−9470.
(53) Peverati, R.; Truhlar, D. G. M11-L: A Local Density Functional That Provides Improved Accuracy for Electronic Structure Calculations in Chemistry and Physics. *J. Phys. Chem. Lett.* **2012**, *3*, 117−124.
(54) Shoji, M.; Koizumi, K.; Kitagawa, Y.; Kawakami, T.; Yamanaka, S.; Okumura, M.; Yamaguchi, K. A General Algorithm for Calculation of Heisenberg Exchange Integrals J in Multispin Systems. *Chem. Phys. Lett.* **2006**, *432*, 343−347.
(55) Shoji, M.; Koizumi, K.; Hamamoto, T.; Kitagawa, Y.; Yamanaka, S.; Okumura, M.; Yamaguchi, K. Hybrid-density Functional Study of Magnetism and Ligand Control in Ni_9 Complexes. *Chem. Phys. Lett.* **2006**, *421*, 483−487.

https://doi.org/10.1021/acs.inorgchem.1c01345
Inorg. Chem. 2021, 60, 16103−16110